

Article

Upper Critical Field and Tunneling Spectroscopy of Underdoped Na(Fe,Co)As Single Crystals

Leonid Morgun ¹, Svetoslav Kuzmichev ^{1,2}, Igor Morozov ³, Alena Degtyarenko ¹, Andrey Sadakov ¹, Andrey Shilov ¹, Ilya Zhuvagin ¹, Yevgeny Rakhmanov ^{1,3} and Tatiana Kuzmicheva ^{1,*}

¹ Lebedev Physical Institute, Russian Academy of Sciences, 119991 Moscow, Russia; morgunla@lebedev.ru (L.M.); kuzmichev@mig.phys.msu.ru (S.K.)

² Faculty of Physics, Lomonosov Moscow State University, 119991 Moscow, Russia

³ Department of Chemistry, Lomonosov Moscow State University, 119991 Moscow, Russia

* Correspondence: kuzmichevate@lebedev.ru

Abstract: A comprehensive study of superconducting properties of underdoped NaFe_{0.979}Co_{0.021}As single crystals by a combination of upper critical field measurements and incoherent multiple Andreev reflection effect (IMARE) spectroscopy is presented. The $H_{c2}(T)$ temperature dependences are measured at magnetic fields up to 16 T with in-plane and out-of-plane field directions and considered within single-band and two-band models in order to estimate the $H_{c2}(0)$ value. In IMARE spectroscopy probes, the magnitude, characteristic ratio, and temperature dependence of the superconducting order parameters ($\Delta_{L,S}(T)$) are determined locally and directly. A possible k -space anisotropy of the large superconducting gap is demonstrated. We show that usage of a quadruple of λ_{ij}^0 coupling constants obtained in the IMARE experiment can significantly reduce the number of free parameters required to fit the $H_{c2}(T)$ dependence within a two-band approach (from six to two).

Keywords: unconventional superconductivity; alkali-metal pnictides; single-crystal growth; magnetotransport; upper critical field; tunneling spectroscopy; Andreev spectroscopy



Citation: Morgun, L.; Kuzmichev, S.; Morozov, I.; Degtyarenko, A.; Sadakov, A.; Shilov, A.; Zhuvagin, I.; Rakhmanov, Y.; Kuzmicheva, T. Upper Critical Field and Tunneling Spectroscopy of Underdoped Na(Fe,Co)As Single Crystals. *Materials* **2023**, *16*, 6421. <https://doi.org/10.3390/ma16196421>

Academic Editors: Kévin Berger and Frederic Trillaud

Received: 31 August 2023

Revised: 20 September 2023

Accepted: 21 September 2023

Published: 27 September 2023



Copyright: © 2023 by the authors. Licensee MDPI, Basel, Switzerland. This article is an open access article distributed under the terms and conditions of the Creative Commons Attribution (CC BY) license (<https://creativecommons.org/licenses/by/4.0/>).

1. Introduction

Layered pnictides Na(Fe,Co)As relate to the so-called 111 family of the iron-based superconductors [1,2]. The 111 family of alkali-metal-based superconducting (SC) pnictides, with LiFeAs and NaFeAs as representative members, has attracted the attention of theoreticians and experimenters due to its unique set of properties that are not typical of other families of iron-based SC (for a review, see [3]). For example, NaFeAs shows superconductivity even in a stoichiometric state with rather low $T_c \approx 10$ K [4,5]. Above this T_c , antiferromagnetic (AFM) and nematic phases develop at $T_m \approx 43$ K and $T_s \approx 55$ K, respectively. Under a partial substitution of Fe by transition metal (Tm) [3], the critical temperature of NaFe_{1-x}Tm_xAs reaches a maximum of $T_c \approx 22$ K simultaneously with AFM and nematicity suppression. A number of probes [6–9] show a natural phase separation in underdoped NaFe_{1-x}Tm_xAs, with clusters of tetragonal SC phase and orthorhombic AFM phase coexisting in the bulk single crystal. With electron doping, the volume fraction of AFM clusters gradually decreases, whereas the optimally doped NaFe_{1-x}Tm_xAs crystal is fully occupied by the SC phase [6–8]. The Fermi surface of NaFe_{1-x}Tm_xAs consists of hole barrels around the Γ point of the first Brillouin zone and electron barrels near the M point [10,11], where several SC condensates develop below T_c .

Owing to the difficulties in studying NaFeAs, there has been a lack of available experimental data to date. Due to the rapid (in a few minutes) degradation of NaFeAs in the presence of even trace amounts of H₂O and O₂, sample preparation and experiment should be conducted in a protective atmosphere.

Two-gap superconductivity in Na(Fe,Co)As was confirmed using surface probes (angle-resolved photoemission spectroscopy (ARPES) [11,12] and scanning tunneling

spectroscopy [13,14]) and bulk techniques (specific heat measurements [4,5]). The magnitudes of the large and small SC gaps within the range of the characteristic ratios ($2\Delta(0)/k_B T_c \approx 5\text{--}9$ and $2.5\text{--}4.5$, respectively) were reported (see Figure 6 in [3]). The significant spread of the characteristic ratios of the SC gaps introduced in the Bardeen–Cooper–Schrieffer (BCS) theory and available in the literature to date obviously results from an absence of direct probes of the gap structure of Na(Fe,Co)As.

Two fundamental mechanisms of superconductivity have been suggested: spin-fluctuation Cooper pairing (so-called s^\pm model) [15] and orbital-fluctuation pairing (s^{++} model) [16]. Theoretically, the SC gap structure of NaFeAs could be described by both the s^{++} [17] approach and the s^\pm model [18,19]. s^\pm - and s^{++} -based calculations agree that the dependence of Cooper pair coupling energy ($2\Delta_L$) on the momentum direction (the SC gap anisotropy) in the $k_x k_y$ plane takes place in NaFeAs [17,19], as well as in iron-based superconductors with similar Fermi surface topology [20] and in sister LiFeAs compounds [21–24]. It is interesting to note that a valuable k -space anisotropy of the large SC order parameter was resolved in ARPES probes of underdoped Na(Fe,Co)As [12] that was unobserved by the same research group in overdoped crystals with similar $T_c \approx 18$ K. This fact could point to an influence of the AFM phase on SC properties.

Until now, the upper critical field temperature dependence of Na(Fe,Co)As has been studied in three works only: for compositions with a wide Co doping range [25,26] and for optimal and overdoped crystals [27]. While in [25,27], magnetotransport measurements were performed within the range of $H = 0\text{--}9$ T, in [26], the $H_{c2}(T)$ behavior was probed up to extremely high magnetic fields of about 45 T in parallel and perpendicular directions for Na(Fe,Co)As with various doping degrees. Unfortunately, the abundance of free parameters used in [26] to fit the experimental $H_{c2}(T)$ dependence with a two-band model (a quadruple of λ_{ij}^0 coupling constants with band diffusivities of D_1 and D_2), as well as the absence of a comprehensive study, could make the values of these free parameters ambiguous.

Here, a novel approach that provides a drastic decrease in the number of free parameters (from six to two) used in order to fit the experimental $H_{c2}(T)$ dependence for a multiple-gap superconductor is presented. The grown underdoped NaFe_{0.979}Co_{0.021}As single crystals are studied by a combination of upper critical field and incoherent multiple Andreev reflection effect (IMARE) spectroscopy probes. The $H_{c2}(T)$ dependences are measured at $H \leq 16$ T in two field directions: $H \parallel ab$ and $H \parallel c$. Using IMARE, for the first time, we locally and directly determine the magnitudes and temperature dependences of the SC-order parameters and roughly estimate a quadruple of full coupling constants (λ_{ij}^0). The obtained $H_{c2}(T)$ temperature dependences are described using a two-band approach with estimated λ_{ij}^0 values.

2. Materials and Methods

Single crystals of NaFe_{0.979}Co_{0.021}As of nominal composition were grown by crystallization from melt. All manipulations, such as obtaining the NaAs precursor and initial mixture preparation, as well as storage and preparation of samples for subsequent measurements, were performed in an argon-filled glove box with residual concentrations of water and oxygen less than 0.1 ppm. Then, preliminarily synthesized 0.058 g CoAs and 1.127 g Fe were added to 2.018 g of NaAs. The prepared reaction mixtures were placed in an alumina crucible, which was sealed in a niobium container in order to prevent a loss of alkali metal; then, the niobium container was sealed in an evacuated quartz ampoule. The ampoule was heated up to 1050 °C at a rate of 100 °C/h and held at this temperature for 24 h. Then, the ampoule was cooled down to 400 °C at a rate of 3 °C/h, annealed at this temperature for 24 h, and cooled down to room temperature in a turned-off oven. The grown single crystals were extracted mechanically from the ingot using a Levenhuk DTX 700 microscope (Tampa, FL, USA), then cut to a rectangular plate shape with dimensions of 1.5×2.5 mm². The presence of a single SC phase was confirmed by X-ray diffraction (XRD), as well as resistive and magnetic measurements (Figure 1).

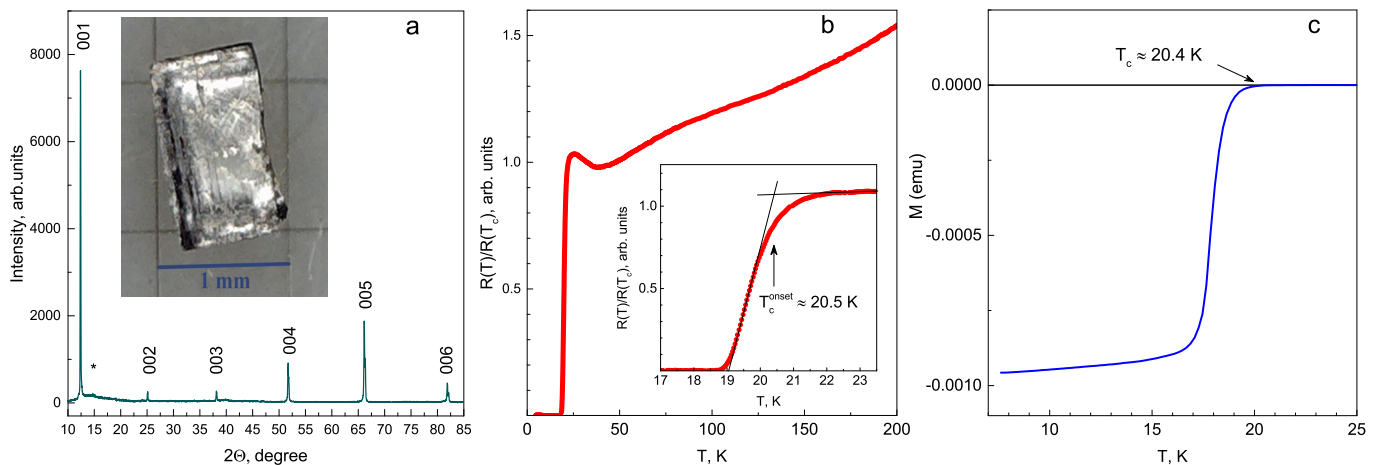


Figure 1. (a) XRD pattern of $\text{NaFe}_{0.079}\text{Co}_{0.021}\text{As}$ single crystal. An image of a plate-like sample cut from a bulk crystal is shown in the inset. Minor feature possibly attributed to the parafilm substrate is marked by *. (b) Temperature dependence of resistance. The inset details the SC transition below $T_c^{\text{onset}} \approx 20.5$ K. (c) Magnetization SC transition with $T_c^{\text{onset}} \approx 20.4$ K.

XRD studies were performed on a Rigaku MiniFlex 600 (Osaka, Japan) with $\text{CuK}\alpha$ radiation in the range of degrees of 5° to 85° (Θ – 2Θ) with a scanning rate of 1° per minute and a step size of 0.02. The sample was placed in an air-sensitive holder in an argon glove box to prevent interaction with air. Figure 1a shows the XRD pattern for grown the $\text{NaFe}_{0.079}\text{Co}_{0.021}\text{As}$ single crystal. All the observed peaks (00l) are sharp and pronounced, demonstrating the homogeneity of the grown crystal and are related to the P4/nmm tetragonal phase. An insignificant halo hump (*) at an angle of 15° can be attributed to the parafilm substrate.

The bulk resistance of the $\text{NaFe}_{0.079}\text{Co}_{0.021}\text{As}$ single crystal within wide temperature range obtained by a four-probe technique is shown in Figure 1b. The SC transition (detailed in the inset of Figure 1b) is observed below $T_c^{\text{onset}} \approx 20.5$ K with a width of $\Delta T_c \approx 1.4$ K. Above T_c , the resistance of the $\text{NaFe}_{0.079}\text{Co}_{0.021}\text{As}$ bulk single crystal falls with increased temperature and reaches a minimum at the temperature of the structural transition ($T_s \approx 36$ K), whereas at higher temperatures, $R(T)$ shows a weak monotonic increase. For the studied crystals, the residual resistivity ratio is rather small: $R(200 \text{ K})/R(T_c) \approx 1.5$. Magnetization $M(T)$ measurements were performed using a SQUID-magnetometer MPMS-XL7 (Quantum Design, San Diego, CA, USA) in fields up to 5 Oe with $H \parallel c$. The resulting $M(T)$ curve (Figure 1c) shows the SC transition at $T_c^{\text{onset}} = 20.4$ K. This critical temperature is similar to that determined by resistive measurements.

Magnetotransport probes were made using a cryogen-free measurement system (CFMS-16). The temperature dependence of the ab -plane resistivity (ρ_{ab}) was determined under a constant magnetic field of up to 16 T along both the ab plane and the c axis. The electric resistivity was measured using the standard four-probe AC lock-in technique with a current of $100 \mu\text{A}$ at a low frequency of 313.1 Hz. All Ohmic contacts were made using silver epoxy, ensuring a resistance of less than 10Ω . To protect the sample from water vapor in the atmosphere, a thin layer of vacuum grease (Apiezon N, Clifton, NJ, USA) was applied to its surface.

In order to directly determine the SC gap structure, we used incoherent the multiple Andreev reflection effect (IMARE). The effect occurs in a symmetrical junction between two SC banks (S) separated by a relatively thin layer of normal metal (n), i.e., an SnS junction. The thickness of such a junction is $d < l$, where l is the inelastic scattering length and d is larger than the SC coherence length (so-called “long” junction). The current–voltage characteristic (CVC) and the dynamic conductance spectrum of the SnS junction in the IMARE regime predicted by [28] are shown in the Appendix A Figure A1a. Below T_c , the related CVC shows an excess current at all bias voltages as compared to the $I(V)$ in the

normal state [28–31]. The corresponding dynamic conductance ($dI(V)/dV$) spectrum shows an enhanced zero-bias conductance (ZBC) peak at $eV \rightarrow 0$ (so-called foot area) [28,30] and a series of $dI(V)/dV$ dips named subharmonic gap structures (SGSs) [28–33]. The SGS positions ($eV_n(T) = 2\Delta(T)/n$, where $n = 1, 2, \dots$) directly determine the magnitude of the SC-order parameter at any temperatures up to T_c [28]. In the case of a multiple-gap superconductor, several SGS would appear in the $dI(V)/dV$ spectrum.

Numerical calculations (see Figure A1b) based on the approach proposed in [34] have shown that in the case of an anisotropic but nodeless SC-order parameter with extended s -wave symmetry, each SGS subharmonic would represent a doublet; the positions of the two $dI(V)/dV$ dips connected by an arch determine the maximum and minimum Cooper pair coupling energies in the k -space: Δ^{out} and Δ^{in} , respectively. In particular, doublet-like Andreev features are reproducibly observed in the $dI(V)/dV$ spectra of SnS junctions in $\text{NaFe}_{0.979}\text{Co}_{0.021}\text{As}$.

SnS junctions based on the $\text{Na}(\text{Fe},\text{Co})\text{As}$ single crystals were formed using a mechanically controlled planar break junction (MCPBJ) technique [35]. The configuration of our experiment, as well as advantages and disadvantages of the technique, are reviewed in [36].

A layered $\text{NaFe}_{1-x}\text{Co}_x\text{As}$ single crystal cut as a thin rectangular plate with typical dimensions of $2 \times 1 \text{ mm}^2$ was mounted onto a U-shaped springy sample holder parallel to the crystallographic ab plane using pads of liquid In–Ga alloy. The sample preparation and mounting were applied in a glovebox with a dry argon atmosphere in order to prevent degradation of the SC properties. Then, the holder was cooled down to $T = 4.2 \text{ K}$ and precisely bent, cracking the crystal on two halves. In the sample, two cryogenic clefts with steps and terraces on the surface separated by a barrier were formed—a kind of superconductor–constriction–superconductor junction—whereas the measurement current always flows along the c direction (the scheme of the resulting junction is shown in Figure A1c). In $\text{NaFe}_{1-x}\text{Co}_x\text{As}$, the tunneling barrier typically obtained using the MCPBJ technique acts as thin normal metal with extremely high transparency of 80–95%, since the observed features of the resulting $I(V)$ and $dI(V)/dV$ curves resemble those predicted theoretically for a highly transparent IMARE regime [28,29].

Below, we summarize the advantages of IMARE spectroscopy of MCPBJ SnS contacts. The implemented technique provides direct local measurement of the magnitude of the SC gaps and their temperature dependences. Owing the clean formed cryogenic clefts, the determined SC gap magnitude is close to its bulk value. Using fine mechanical readjustment, it becomes possible to obtain dozens of SnS junctions with various R_N values in one and the same sample during a single cooldown process. The latter facilitates collection of a large set of statistics, verifying the reproducibility of the data.

3. Results and Discussion

3.1. Upper Critical Field Probes

Figure 2 presents magnetotransport measurements in a static magnetic field for an underdoped $\text{NaFe}_{0.979}\text{Co}_{0.021}\text{As}$ single crystal. The anomaly in the resistivity curve, namely an increase with a decrease in temperature, corresponds to the structural phase transition. The field-induced broadening of the SC transition is negligible for both directions of the magnetic field. In this study, three different criteria of SC critical temperature determination are used: (i) T_c is taken as a temperature corresponding to a 50% resistance drop within the SC transition (hereafter, “50% criterion”); (ii) $dR(T)/dT$ is taken as the maximum temperature (“max dR/dT ” criterion); and (iii) the onset temperature of the SC transition is determined similarly to that shown in the inset of Figure 1b (“ T_c^{onset} ” criterion). The obtained $H_{c2}(T)$ dependences with the temperature determined using the three above mentioned criteria are shown in Figure 3. Note that the obtained $H_{c2}(T)$ dependences are almost linear and show no “tails” in the close vicinity of T_c (observed in Figure 7 in [25]).

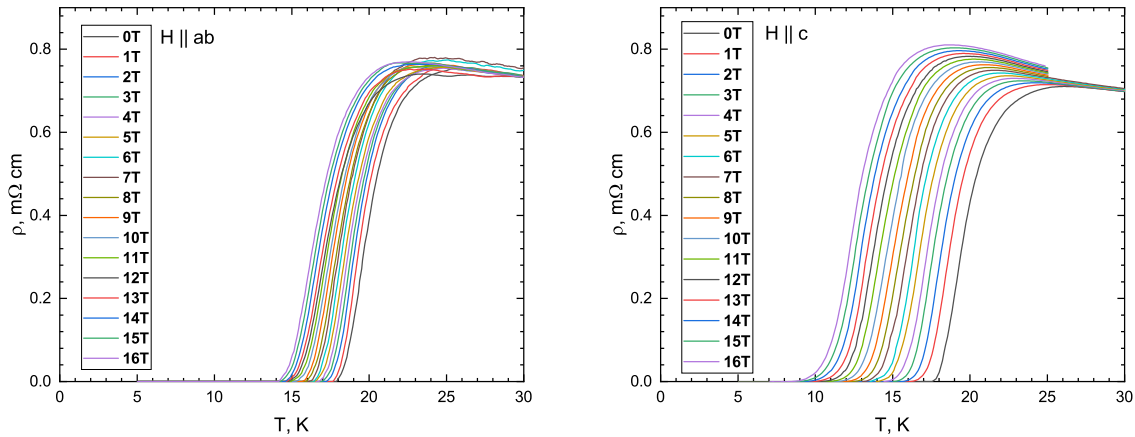


Figure 2. Evolution of temperature dependence of the in-plane resistivity (ρ_{ab}) for $\text{NaFe}_{0.979}\text{Co}_{0.021}\text{As}$ with $H\parallel ab$ and $H\parallel c$ magnetic field directions. In both cases, the field direction is normal to the AC current direction.

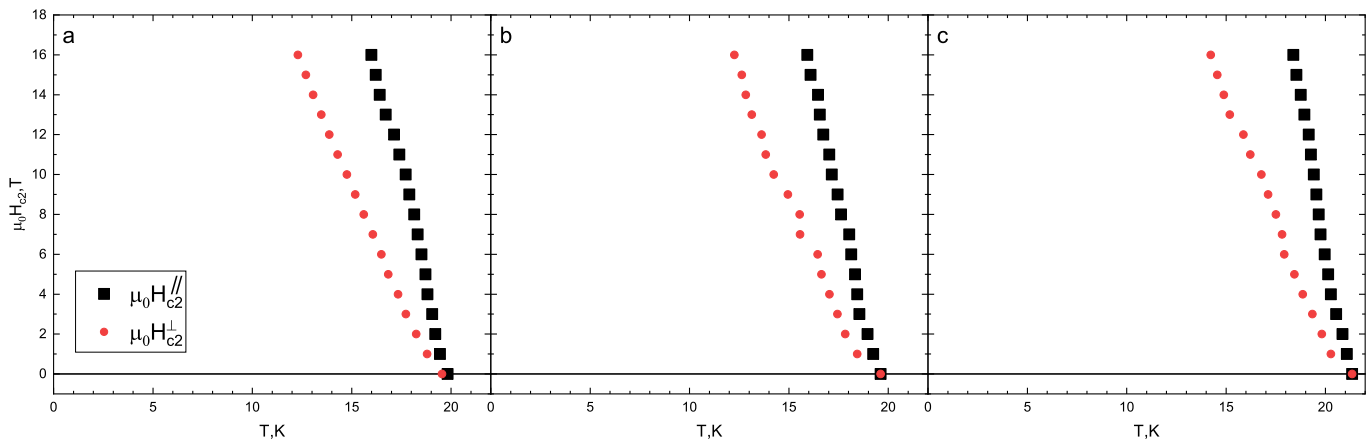


Figure 3. The maximum magnetic field (16 T) is definitely lower than the fundamental $H_{c2}(0)$. As a result, several criteria were employed to determine the $H_{c2}(T)$ temperature dependence in the vicinity of T_c , including the 50% of normal state resistivity criterion (a), the maximum dR/dT criterion (b), and the onset temperature (T_c^{onset}) criterion (c).

According to ARPES measurements [11,37,38] and numerical calculations [39,40], the $\text{Na}(\text{Fe},\text{Co})\text{As}$ compound is a quasi-2D superconductor with a Fermi surface consisting of collinear warped barrels. When a magnetic field is applied parallel to the SC planes, the electrons in the system form open orbits along the cylindrical Fermi surfaces. This results in a negligible orbital effect and a significant increase in the critical field above that expected for a more isotropic superconductor. On the other hand, when the magnetic field is applied perpendicular to the SC planes, closed electron orbits are formed within the Fermi surfaces, leading to the creation of vortices and reducing the orbital limit for the critical field. Therefore, in general, the parallel critical field (H_{c2}^{\parallel}) is greater than the perpendicular critical field (H_{c2}^{\perp}), as observed in our samples (see Figure 3).

In this paper, the studied samples are assumed to be in the dirty limit, where the mean free path (l^{el}) is relatively small and the coherence length (ξ) is of the same order of magnitude as l^{el} . This assumption is supported by the low residual resistivity ratio [41], the low superconducting volume fraction of the parent compound NaFeAs [7], and the tendency for pnictide superconductors to have a small mean free path (l^{el}) due to their low Fermi velocities [42] and high scattering rates. Unfortunately, the mean free path determination using Hall measurements could be ambiguous in the case of metal with

multiple electron and hole bands. The average coherence lengths calculated for the studied samples are $\xi_{ab}(0) \approx 2.5$ nm and $\xi_c(0) \approx 2$ nm (see Table 1).

Table 1. Summary of parameters for the upper critical field (H_{c2}) of the investigated $\text{NaFe}_{0.979}\text{Co}_{0.021}\text{As}$: $H_{c2}(T)$ slopes at $T \rightarrow T_c$, $H \parallel ab$, and $H \parallel c$ directions; magnetic anisotropy $\gamma_H(T \rightarrow T_c) \equiv H_{c2}^{ab}/H_{c2}^c$; estimated zero-temperature values of $H_{c2}(0)$ (where I and II correspond to the one-band and two-band model, respectively); and coherence lengths $\xi_{ab,c}$.

Criterion	$-\frac{dH_{c2}^{ab}}{dT} _{T_c}$ T/K	$-\frac{dH_{c2}^c}{dT} _{T_c}$ T/K	$\gamma_H(T_c)$	$H_{c2}^{I,c}(0)$ T	$H_{c2}^{II,c}(0)$ T	$H_{c2}^{I,ab}(0)$ T	$H_{c2}^{II,ab}(0)$ T	$\xi_{ab}(0)$ nm	$\xi_c(0)$ nm
50%	6.85	2.45	2.8	30	49	58	61	2.59	2.08
$\max dR/dT$	6.34	2.52	2.5	32	52	54	60	2.51	2.18
T_c^{onset}	6.97	2.74	2.54	36	59	60	77	2.36	1.81

Using single-band Werthamer–Helfand–Hohenberg [43] and two-band Gurevich [44] models, the temperature dependencies of H_{c2} were obtained as shown in Figures 4 and 5. Generally, the two-band model in the dirty limit [44] has six free parameters: four “full” coupling constants (λ_{ij}^0 , where λ_{11}^0 and λ_{22}^0 are intraband and λ_{12}^0 and λ_{21}^0 are interband); label 1 relates to a band with “strong” SC condensate, and label 2 relates to one where the “weak” SC condensate develops, with band diffusivities of D_1 and D_2 . In order to reduce the number of free parameters, we used the same coupling constants as in [26]: $\lambda_{11} = \lambda_{22}^0 = 1$, $\lambda_{11}^0 \lambda_{22}^0 - \lambda_{12}^0 \lambda_{21}^0 = 0.5$. For H_{c2}^c , the resulting diffusivity ratio ($\frac{D_1}{D_2} \approx 6$) does not change for the three different T_c criteria. This value is higher than the $\frac{D_1}{D_2} \approx 2.5$ obtained in [26] for the sample with 2% Co concentration, for which our $\frac{D_1}{D_2} \approx 6$ satisfies the general increasing tendency of the diffusivity ratio with doping observed in Figure 5b in [26].

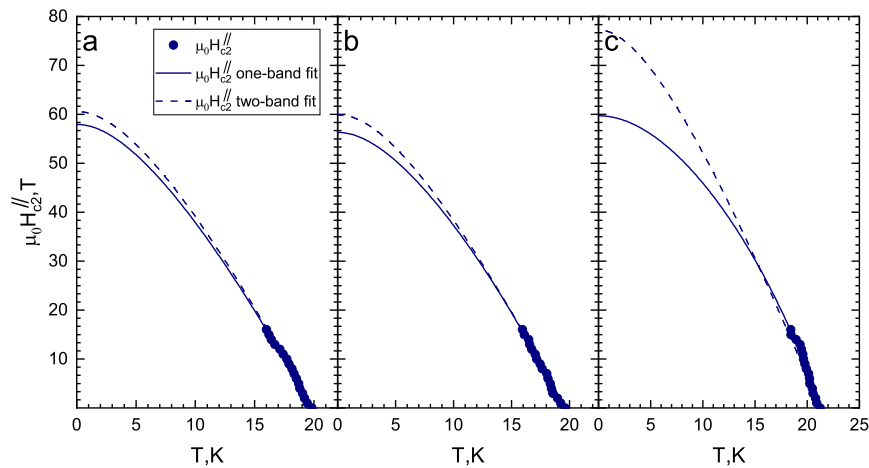


Figure 4. Temperature dependence of the upper critical fields (H_{c2}^{\parallel}) obtained in the framework of a single-band WHH model (solid lines) and two-band Gurevich model (dashed lines): (a) 50% criterion; (b) $\max dR/dT$; (c) T_c^{onset} .

However, for H_{c2}^c , the two-band model can fit data by setting $D_1 = D_2$, similarly to that obtained in [26]. In Figure 5d, we present the $H_{c2}(T)$ fit using two sets of full coupling constants estimated in the IMARE experiment (corresponding to different Coulomb repulsion strengths): set a: $\lambda_{11}^0 = 0.435$, $\lambda_{22}^0 = 0.326$, $\lambda_{12}^0 = 0.236$, and $\lambda_{21}^0 = 0.133$ (solid line); set b: $\lambda_{11}^0 = 0.412$, $\lambda_{22}^0 = 0.304$, $\lambda_{12}^0 = 0.219$, and $\lambda_{21}^0 = 0.108$ (dotted line) (see Section 4). In the latter case, the determined diffusivity ratios are $\frac{D_1}{D_2} \approx 3.52$ and 3.75 , respectively.

Both single-band and two-band fits describe the experimental data quite well (see Figures 4 and 5). Nevertheless, the determined $H_{c2}^c(0)$ value depends on the model (about 15%). The obtained estimates for the upper critical fields ($H_{c2}^c(0)$, $H_{c2}^{ab}(0)$) and slopes ($-\frac{dH_{c2}^c}{dT}|_{T_c}$, $-\frac{dH_{c2}^{ab}}{dT}|_{T_c}$) are given in Table 1. The resulting $-\frac{dH_{c2}^c}{dT}|_{T_c} \approx 2.5\text{--}2.7\text{ T/K}$ are very close to the related values determined in [25,26] for 2.5% and 2% Co samples, respectively, whereas our $-\frac{dH_{c2}^{ab}}{dT}|_{T_c} \approx 6.3\text{--}7.0\text{ T/K}$ values appear to be a slightly lower than that reported in [26] but higher than that reported in [25]. The resulting anisotropy of the upper critical field in the vicinity of T_c is $\gamma_H(T \rightarrow T_c) \equiv \frac{H_{c2}^{ab}}{H_{c2}^c} \approx 2.5\text{--}2.8$ and resembles the $\gamma_H(T \rightarrow T_c) \approx 3$ value obtained in [26] and exceeds the $\gamma_H(T \rightarrow T_c) \approx 2.25$ estimated in [25] for an underdoped $\text{NaFe}_{1-x}\text{Co}_x\text{As}$ crystal of similar composition.

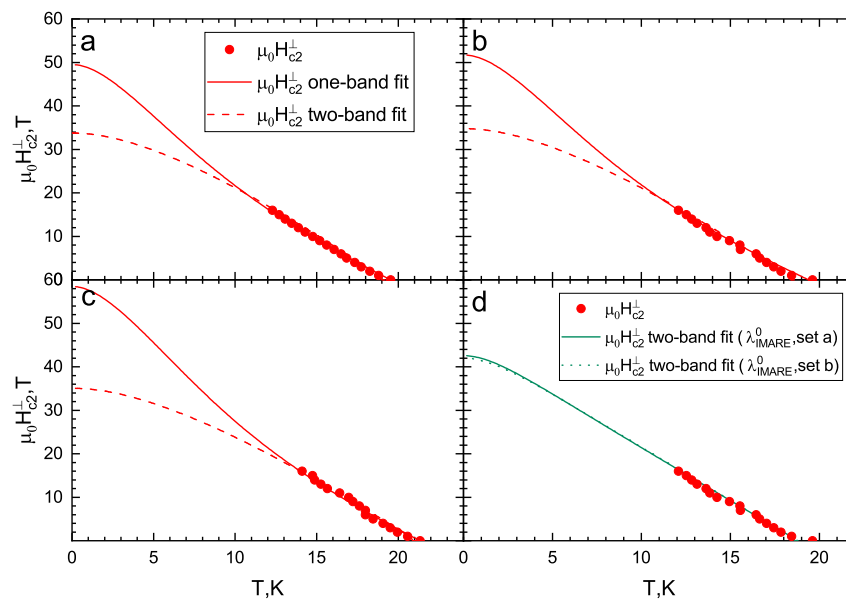


Figure 5. Temperature dependence of the upper critical fields (H_{c2}^{\perp}) obtained in the framework of a single-band WHH model (solid lines) and two-band Gurevich model (dash lines) with $\lambda_{11}^0 = \lambda_{22}^0 = 1$ and $\lambda_{11}^0 \lambda_{22}^0 - \lambda_{12}^0 \lambda_{21}^0 = 0.5$ taken from [26] under various critical temperature criteria: (a) 50% criterion; (b) max dR/dT ; (c) onset of SC transition. (d) Temperature dependence of the upper critical field (H_{c2}^{\perp}) determined by max dR/dT and two-band Gurevich models with $\lambda_{11}^0 = 0.435$, $\lambda_{12}^0 = 0.236$, $\lambda_{21}^0 = 0.133$, and $\lambda_{22}^0 = 0.326$ (solid line) and $\lambda_{11}^0 = 0.412$, $\lambda_{12}^0 = 0.219$, $\lambda_{21}^0 = 0.108$, and $\lambda_{22}^0 = 0.304$ (dotted line) (these two λ_{ij}^0 sets are derived from the renormalized λ_{ij} estimated in the IMARE experiment: $D_1/D_2 \approx 3.52$ and 3.75 , respectively).

For both field directions, since the temperature associated with a 50% $R(T)$ drop almost coincides with that corresponding to max dR/dT , these two criteria of T_c determination yield similar $H_{c2}(0)$ values, both lower than the $H_{c2}(0)$ estimated using the “ T_c^{onset} criterion”. Generally, the temperature attributed to $dR(T)/dT$ maximum indicates the transition of the main volume of the crystal to the SC state. Therefore, the $H_{c2}(0)$ values determined using the “max dR/dT ” criterion seem to be physically correct.

The single-band WHH estimate provides the range of zero-temperature values between $\mu_0 H_{c2}^c(0) \approx 30\text{--}36\text{ T}$ (depending on the chosen criterion) and $\mu_0 H_{c2}^{ab}(0) \approx 54\text{--}60\text{ T}$. The small increase in $H_{c2}^{ab,c}(0)$ estimated using the two-band fit as compared to that obtained by the single-band WHH model is caused by a “weak” SC condensate contribution to the upper critical field at low temperatures.

3.2. IMARE Spectroscopy

Figure 6a shows the CVC of MCPBJ contact measured in the SC and the normal states at $T = 4.2$ K and 21.5 K, respectively. The local critical temperature of this junction corresponding to the contact area transition to the normal state is $T_c \approx 19.8$ K (see below). Below T_c , the supercurrent branch at $eV = 0$ is absent in the CVC; instead, a foot area with enhanced dynamic conductance appears in the corresponding $dI(V)/dV$ spectrum shown in Figure 6b. At 4.2 K (red curve in Figure 6a), an excess current presents in the CVC as compared to that above T_c (blue line), tending toward a constant value at high bias voltages. The observed CVC features at $T \ll T_c$ are typical for a “long” SnS junction with incoherent transport and high transparency of the barrier, in accordance with all theoretical models describing the multiple Andreev reflection effect [28–33].

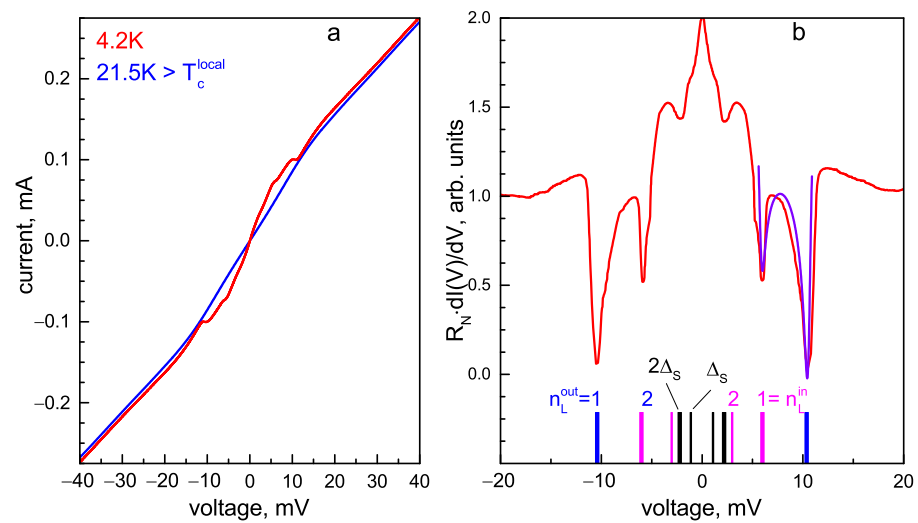


Figure 6. (a) Current–voltage characteristic of SnS junction in underdoped $\text{NaFe}_{1-x}\text{Co}_x\text{As}$ at temperatures below and above T_c (red and blue lines, respectively). (b) Corresponding dynamic conductance spectrum measured at $T = 4.2$ K. The monotonic background is suppressed for clarity. Vertical bars show the positions of the Andreev features of $\Delta_L^{\text{out}}(0) \approx 5.2$ meV (blue bars, $n_L^{\text{out}} = 1, 2$ labels), $\Delta_L^{\text{in}} \approx 3.1$ meV (magenta bars, $n_L^{\text{in}} = 1, 2$ labels), and the small SC gap of $\Delta_S(0) \approx 1.1$ meV (black bars). The violet line fits the shape of the doublet with model presented in [34] for a case of extended s -wave symmetry of the large SC gap (Δ_L).

In the normal state, all the $I(V)$ features caused by IMARE vanish, but the CVC remains slightly nonlinear, showing the unconventional nature of $\text{NaFe}_{1-x}\text{Co}_x\text{As}$. The resembling $I(V)$ nonlinearity is reproducible and cannot be caused by a junction overheating during the current flow or any geometrical resonance, since a random contact dimension is obtained by the MCPBJ technique (for details, see Figure 1 in [45]). On the contrary, the nonlinear $I(V)$ normal-state behavior may originate from the features of the electron density of $N(E)$ states in the vicinity of the Fermi level [46] caused by either specific band structure topology or resonant electron–boson interaction, which requires further studies.

The corresponding $dI(V)/dV$ spectrum measured at $T \ll T_c$ (Figure 6b) shows a series of dips. The pronounced minima located at $|eV| \approx 10.4$ and 6.2 meV do not satisfy the subharmonic positions as $n = 1, 2$ or $n = 2, 3$ numbers and therefore cannot be attributed to one and the same SGS caused by a single SC gap. At higher bias voltages, the $dI(V)/dV$ spectrum has no features caused by the SC state. Hence, we consider this doublet as the fundamental ($n = 1$) Andreev feature, the position of which directly determines two SC-order parameters: $2\Delta_L^{\text{out}} \approx 10.4$ meV and $2\Delta_L^{\text{in}} \approx 6.2$ meV (bold blue and magenta bars, respectively; $n_L^{\text{in,out}}$ labels in Figure 6b). A minor feature at $|eV| \approx 5.2$ meV could be interpreted as a second subharmonic ($n_L^{\text{out}} = 2$) of Δ_L^{out} . The position of the $n_L = 2$ Andreev feature caused by the Δ_L^{in} order parameter expected at $|eV| \approx 3.1$ meV is not resolved, since

it merges with the fundamental harmonic ($n_S = 1$) of the small SC gap ($2\Delta_S \approx 2.2$ meV) and therefore possibly smears it. At lower bias voltages, the second Δ_S subharmonic is also visible (thin black bars, Δ_S labels in Figure 6b).

The typical arch-like shape of the doublet could be fitted within the approach proposed in [34] for a case of SC gap with extended s -wave symmetry of $\cos(4\theta)$ type without nodes (compare the experimental $dI(V)/dV$ and the blue line fit in Figure 6b). Therefore, the observed doublet could be interpreted as a wide Andreev feature of a single SC-order parameter developing below T_c on one and the same Fermi surface sheet with a moderate anisotropy in the k space. In this very probable case, the directly determined SC energy parameters (Δ_L^{in} and Δ_L^{out}) could be considered as the gap edges; the minimum and maximum Cooper pair coupling energies in this band depend on the momentum direction in the $k_x k_y$ plane. The less probable scenario is that the determined $2\Delta_L^{\text{out}}$ and $2\Delta_L^{\text{in}}$ could represent two distinct SC-order parameters characterizing the properties of two SC condensates developed in different bands (see Section 4).

The complex structure observed in the $dI(V)/dV$ characteristics of SnS junctions with random geometry is reproducible. Figure 7a,b show a set of CVCs and the corresponding dynamic conductance spectra of SnS junctions with normal resistances of $R_N \approx 50$ –175 Ohm formed in the single crystals from the same batch. The R_N value depends on the contact dimensions and transparency of the barrier, and can generally change from one contact point to another. Despite such a wide R_N range, the positions of all IMARE features in the corresponding $dI(V)/dV$ spectra remain almost constant. In Figure 7b, the positions of the doublet (blue and magenta bars, $2\Delta_L$ labels) directly determine the SC-order parameters ($2\Delta_L^{\text{out}}(0) \approx 10.4$ meV and $2\Delta_L^{\text{in}}(0) \approx 6.6$ meV). In the two upper spectra in Figure 7b, the second ($n = 2$) Andreev subharmonic also forms a well-resolved doublet (thin blue and magenta bars, Δ_L labels). According to the formula of SGS, it is located at a position two times smaller than that of the fundamental one. The Andreev feature of the small SC gap is present in the two bottom curves as a dip located at $|eV| \approx 2.4$ meV and corresponds to the $2\Delta_S(0) \approx 2.4$ meV magnitude. This $2\Delta_S$ feature is possibly undistinguished in the red and dark yellow upper spectra in Figure 7b due to its merging with the SGS of Δ_L^{in} . A representative set of the $dI(V)/dV$ arch-like doublets (of the fundamental $n = 1$ feature) obtained in different underdoped $\text{NaFe}_{1-x}\text{Co}_x\text{As}$ single crystals from the same batch is shown in Figure 7c.

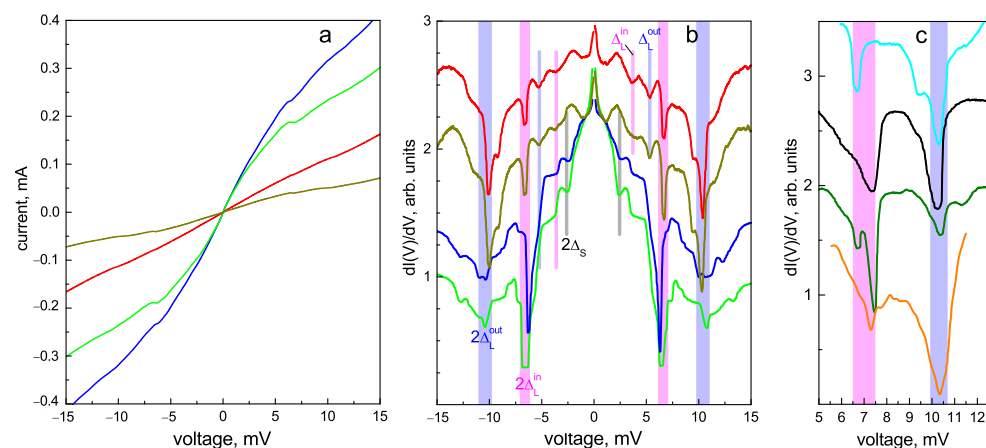


Figure 7. (a) Current–voltage characteristics of SnS junctions with different normal resistance (R_N) values at $T = 4.2$ K obtained in various underdoped $\text{NaFe}_{1-x}\text{Co}_x\text{As}$ single crystals from the same batch. (b) Corresponding dynamic conductance spectra measured at $T = 4.2$ K. Vertical blue and magenta bars show the positions of the Andreev dips of $2\Delta_L^{\text{out}}(0) \approx 10.4$ meV and $2\Delta_L^{\text{in}} \approx 6.6$ meV, respectively. Gray lines point to the fundamental Andreev dip of the small SC gap ($2\Delta_S(0) \approx 2.4$ meV). (c) Fragments of $dI(V)/dV$ spectra for various contacts measured at $T = 4.2$ K, reproducibly showing a doublet Andreev feature of the large SC gap.

The large IMARE data obtained with underdoped $\text{NaFe}_{1-x}\text{Co}_x\text{As}$ are shown in Figure 8. The presented data involve the energy parameters of SnS junctions with local critical temperatures $T_c \approx 19\text{--}22\text{ K}$ (the temperature of the contact area transition to the normal state). In order to account for the Δ_i variation within the obtained T_c range, the values of characteristic ratios $2\Delta_i(0)/k_B T_c$ are compared and summarized in color histogram (Figure 8a). The data are presented as semitransparent bars positioned along the horizontal axis corresponding to the characteristic ratios of all SC-order parameters obtained by us (the vertical axis does not matter), whereas the area of the most intensive color points corresponds to the most frequently observed experimental value. For the two largest SC-order parameters, the characteristic ratios are $2\Delta_L^{\text{out}}(0) \approx 6.0 \pm 0.3$ and $2\Delta_L^{\text{in}}(0)/k_B T_c \approx 3.9 \pm 0.5$. Supposing $\Delta_L^{\text{in,out}}$ as the edges of one and the same anisotropic SC-order parameter Δ_L , its possible anisotropy in the momentum space can be estimated as $A_L \approx 28\text{--}43\%$ (Figure 8b). For the small SC gap, the characteristic ratio ($2\Delta_S(0)/k_B T_c \approx 1.4\text{--}2.0$) appears below the weak coupling BCS limit 3.5, which is typical for a “weak” SC condensate in a multiple-gap superconductor.

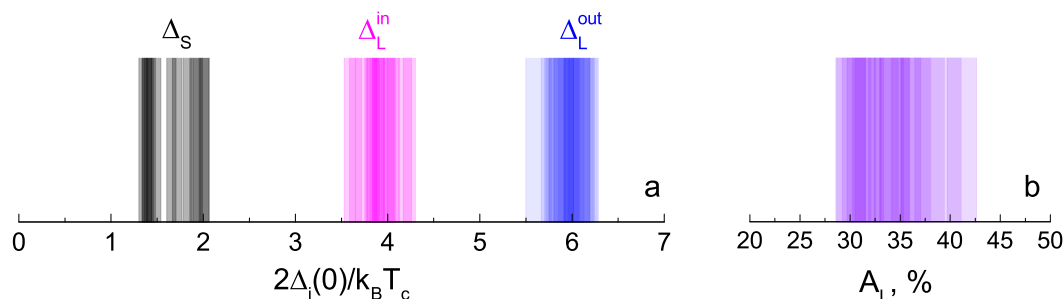


Figure 8. (a) Color histogram of the characteristic ratios ($2\Delta_i(0)/k_B T_c$) of the determined SC-order parameters (Δ_L^{out} , Δ_L^{in} , and Δ_S) at $T \ll T_c$. The data were obtained with underdoped $\text{NaFe}_{1-x}\text{Co}_x\text{As}$ single crystals from the same batch, and the range of local critical temperatures of the SnS junctions was 19–22 K. Each value is shown by a semitransparent bar (blue, magenta, or black), whereas the position (along the horizontal axis) of the most intense color corresponds frequency of experimental attainment. (b) Color histogram for the possible Δ_L anisotropy value taken as $A_L \equiv 100\% \cdot [1 - \Delta_L^{\text{in}}/\Delta_L^{\text{out}}]$.

Consider the temperature evolution of the SC gap structure in the $dI(V)/dV$ spectrum of the SnS junction (as presented in Figure 6) shown in Figure 9a. The $dI(V)/dV$ curves shown in Figure 9a are manually offset vertically for clarity, whereas the normal resistance (R_N) of the junction remains almost constant, with the temperature pointing to ballistic transport through this junction (compare the red and blue CVCs parallel at $eV \gg 2\Delta(0)$ in Figure 6a). With increased temperature, the zero-bias conductance peak shrinks, whereas all the Andreev features become less intense and shift toward zero bias, driven by the reduction in the number of Cooper pairs. At $T \approx 21.5\text{ K} > T_c$ (upper pink curve in Figure 9a), all the IMARE-caused features vanish in the $dI(V)/dV$ spectrum, indicating the transition of the contact area to the normal state and the absence of Cooper pairs.

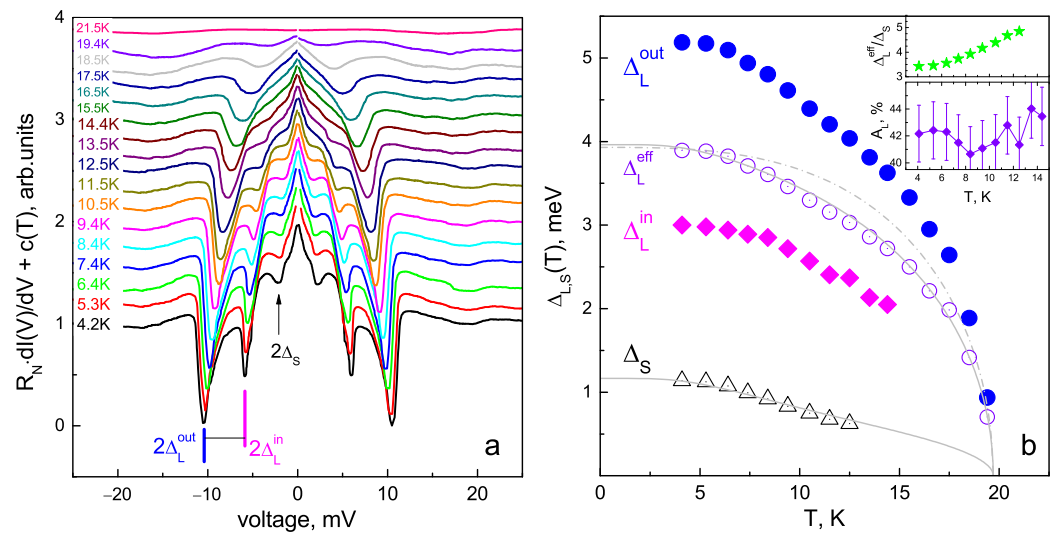


Figure 9. (a) Evolution of the $dI(V)/dV$ spectrum shown in Figure 6 with temperature. The curves are manually shifted along the vertical axis for clarity by $c(T)$. (b) Temperature dependences of the SC-order parameters ($\Delta_L^{\text{out}}(T)$, $\Delta_L^{\text{in}}(T)$, and $\Delta_S(T)$) directly determined using panel data (a) (solid circles, rhombs, and open triangles, respectively). The effective large SC gap determined as $\Delta_L^{\text{eff}} \equiv \sqrt{\Delta_L^{\text{out}} \cdot \Delta_L^{\text{in}}}$ is shown by open circles. Single-band BCS-like behavior (dash-dot line) and two-band fits using Moskalkenko and Suhl equations with renormalized BCS integrals (gray solid line) are shown for comparison. **The upper inset** presents the ratio between Δ_L^{eff} and Δ_S vs. temperature, and the **lower inset** shows the temperature dependence of the possible anisotropy of Δ_L .

Temperature dependences ($\Delta_L^{\text{in,out}}(T)$) directly determined using the evolution of the $dI(V)/dV$ doublet position are shown in Figure 9b by solid magenta rhombs and blue circles, respectively. The lower inset presents the temperature dependence of the possible large gap anisotropy: $A_L \approx 42\% \approx \text{const}$ hardly evolves with temperature, which results in quite similar temperature behavior of Δ_L^{in} and Δ_L^{out} . In order to designate the effective value of the large SC gap, we take its zero-temperature value as $\Delta_L^{\text{eff}}(0) \equiv \sqrt{\Delta_L^{\text{in}}(0)\Delta_L^{\text{out}}(0)}$ and associate it with the $\delta_L^{\text{out}}(T)$ temperature trend ($\delta(T) \equiv \Delta(T)/\Delta(0)$); the resulting $\Delta_L^{\text{eff}}(T)$ dependence is shown in Figure 9b by open violet circles. Starting from $T \approx 5\text{--}6\text{ K}$, the small SC gap decreases a slightly more rapidly compared to the large one. The $\Delta_L^{\text{eff}}(T)/\Delta_S(T)$ ratio increases with temperature, as shown by the green stars in the upper inset of Figure 9b. Due to differing temperature behavior, we attribute the corresponding low-bias $dI(V)/dV$ features as Andreev subharmonics of a distinct Δ_S -order parameter.

The dependence of Δ_L^{eff} on temperature roughly resembles a standard single-band BCS-like function (dash-dot line in Figure 9b) but slightly bends down at $T \approx 5\text{--}18\text{ K}$. The small SC gap shows more significant curving, which is typical for a multiple-gap SC with moderate interband coupling (comparable to intraband coupling). As a rough estimate, the $\Delta_L^{\text{eff}}(T)$ and $\Delta_S(T)$ temperature dependences were fitted using a two-band model based on Moskalkenko and Suhl et al.'s system of equations [47–49] with renormalized temperatures in two BCS integrals [50]. We used the experimental values of T_c and $\Delta_i(0)$ and the two free parameters: $\alpha = \lambda_{12}/\lambda_{21}$, $\beta = \sqrt{\lambda_{11}\lambda_{22}}/\sqrt{\lambda_{12}\lambda_{21}}$; other parameters were calculated using the equations mentioned above. The resulting fits are in agreement with the experimental data (solid gray lines in Figure 9b).

Using a two-band fit, the estimated quadruple of renormalized or “weak” coupling constants is $\lambda_{11} = 0.292$, $\lambda_{22} = 0.184$, $\lambda_{12} = 0.098$, $\lambda_{21} = 0.022$. Due to abundance of free parameters, extraction of full coupling constants (λ_{ij}^0) becomes ambiguous.

4. Discussion

Since the Andreev features of Δ_S are located on the notably sloped $dI(V)/dV$ background (at the foot area caused by Δ_L condensate), determination of its exact positions is complicated, resulting in increased diversity of the corresponding characteristic ratio as compared to that of the large SC gaps. Another reason for this could be the possible anisotropy of the small SC gap. No clear doublets of Δ_S are reproducibly observed in the $dI(V)/dV$ spectra, which could be a sign of either the s -wave symmetry type of the small SC gap, its strong anisotropy ($A_S > 50\%$), or even nodal distribution ($A_S = 100\%$) in the momentum space. Since the ZBC value is determined by the structure of both SC-order parameters, it is impossible to make a judgment about the presence of nodes for a small gap.

All the determined $2\Delta_i(0)/k_B T_c$ values are reproducible and do not depend on the normal resistance of the corresponding SnS junction (which is random), as shown in Figure 10a. Therefore, the energy parameters directly determined in our IMARE experiment do not depend on the contact geometry, and the proportion of ballistic-to-diffusive transport reflects the bulk properties of the SC subsystem of $\text{NaFe}_{1-x}\text{Co}_x\text{As}$ and cannot be attributed to dimensional effects or artefacts. Accordingly, the characteristic ratios for the three SC-order parameters remain almost independent at the local critical temperature within the studied $T_c \approx 19\text{--}22\text{ K}$ range (Figure 10b), which indicates a scaling between Δ_L^{out} , Δ_L^{in} , and Δ_S with local T_c .

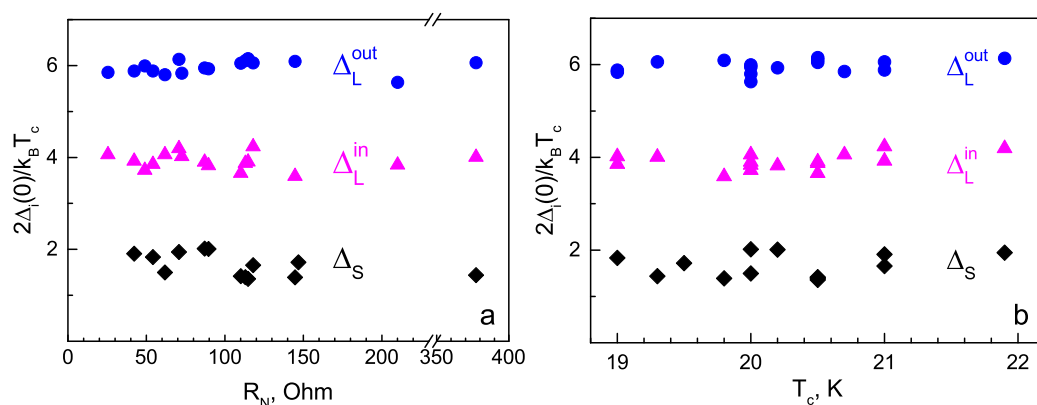


Figure 10. The dependences of the SC-order parameter characteristic ratios on the normal resistance (R_N) of contacts under study (a) and on the local critical temperature (T_c) of the junction (b).

Noteworthy, in the IMARE experiment, only the energy parameters (Δ_i) of the SC state and their temperature dependences were directly determined, rather than the symmetry type or sign of the SC gap. As mentioned above, the arch-like doublets reproducibly observed in the $dI(V)/dV$ spectra could be caused by a single Δ_L SC gap with k -space anisotropy. Less probable is the possibility of two isotropic SC gaps (Δ_L^{in} and Δ_L^{out}) developing in different bands. In order to directly distinguish between the abovementioned possibilities, additional theoretical and experimental studies are necessary. Therefore, the possible anisotropy of the large SC gap remains ambiguous.

Nonetheless, several issues can be highlighted that favor the anisotropy scenario. First, as mentioned above, the SC gap anisotropy is generally supposed for $\text{NaFe}_{1-x}\text{Co}_x\text{As}$, as well as for other families of iron-based superconductors in the framework of both the s^\pm and s^{++} approaches [17,18,20]. Secondly, the shape of the doublet representing two dips connected by an arch resembles that numerically calculated for an SC-order parameter with extended s -wave symmetry of the $\cos(4\theta)$ type without nodes (violet line fit in Figure 6c; see also the magenta theoretical curve in Figure A1b). Moreover, the relative width of the doublet remains almost constant with temperature (see the inset of Figure 9b), providing $\Delta_L^{\text{in}}(T)/\Delta_L^{\text{out}}(T) \approx \text{const}$.

This behavior resembles the temperature evolution of similar dynamic conductance doublets reproducibly observed by us earlier in sister LiFeAs compound [51], as well as

BaFe_{2-x}Ni_xAs pnictides [52]. Generally, in a multiple-gap SC, the $\Delta_1(T)/\Delta_2(T) \approx const$ behavior takes place in the only case of $\det(\lambda_{ij}) = 0$, yielding $\beta = 1$. Since the realization of this exact case in NaFe_{1-x}Co_xAs and the abovementioned LiFeAs and BaFe_{2-x}Ni_xAs seems less probable, one could consider the observed $A_L \approx const$ dependence as favoring our suggestion about the realization of k -space anisotropy of the large SC gap. Additionally, the estimated $A_L \approx 28$ –43% is close to the large SC gap anisotropy ($\approx 30\%$) determined by ARPES [12].

Since electron–phonon coupling seems rather weak in Fe-based superconductors [53], we did not use the phonon renormalization term $(1 + \lambda_{ij})$, determining $\lambda_{ij}^0 = \lambda_{ij} + \mu_{ij}^*$, where μ_{ij}^* are Coulomb pseudopotentials. The cutoff energy was taken as $\omega_c = 40$ meV. As a result, one could obtain two sets of full coupling constants: set (a): $\lambda_{11}^0 = 0.412$, $\lambda_{22}^0 = 0.304$, $\lambda_{12}^0 = 0.219$, and $\lambda_{21}^0 = 0.108$ for a weak Coulomb repulsion with free parameter $\mu_{eff}^* = 0.112$; set (b): $\lambda_{11}^0 = 0.435$, $\lambda_{22}^0 = 0.326$, $\lambda_{12}^0 = 0.236$, and $\lambda_{21}^0 = 0.133$ (the used coupling constant sets are labeled as λ_{IMARE}^0 in Figure 5d) for a moderate Coulomb repulsion with a reasonable $\mu_{eff}^* = 0.134$ (this value is similar to that calculated in [54] for NaFeAs). Free choice of $\mu^* > 0.2$ seems hardly eligible unless there is a specific reason. For the two obtained quadruples of λ_{ij}^0 , the estimated ratio between the normal-state band density of state N_i near the Fermi level are $\alpha \equiv N_2/N_1 \approx 2$ and 1.8, and the intraband-to-interband coupling strengths are $\beta \approx 2.3$ and 2.1 for sets (a,b), respectively.

The two obtained sets of full coupling constants were used to fit the upper critical field temperature dependence with the two-band Gurevich model [44]. As experimental data, the $\mu_0 H_{c2}^\perp(T)$ dependence obtained with the $\max dR/dT$ criterion was used as follows. First, the corresponding T_c coincides with the local critical temperature of the studied SnS junction shown in Figure 9. Secondly, since our IMARE experiment with planar junctions generally provides information about the SC gap anisotropy in the $k_x k_y$ -plane, the obtained SC properties should be compared with the upper critical field ($\mu_0 H_{c2}^\perp(T)$), which is determined by the in-plane coherence length (ξ_{ab}). Both λ_{IMARE}^0 sets can fit the linear $\mu_0 H_{c2}^\perp(T)$ fading in the vicinity of T_c and yield a zero temperature value ($\mu_0 H_{c2}^\perp(0) \approx 42$ T). The strength of Coulomb repulsion does not seriously affect the resulting fit.

5. Conclusions

Underdoped NaFe_{0.979}Co_{0.021}As SC pnictide single crystals with a critical temperature of $T_c \approx 20.5$ K were grown using a “self-flux” technique. Using magnetotransport probes, the temperature dependences of the upper critical field ($H_{c2}(T)$) were measured within the range of $H \leq 16$ T in two field orientations, and the slopes ($-\frac{dH_{c2}^{ab}}{dT}|_{T_c} \approx 6.34$ –6.97 and $-\frac{dH_{c2}^c}{dT}|_{T_c} \approx 2.45$ –2.74 (depending on the T_c criterion)) were determined. The experimental $H_{c2}(T)$ dependences can be fitted with both the WHH and Gurevich models, with estimated $H_{c2}^{ab}(0)$ and $H_{c2}^c(0)$ up to 77 and 59 T, respectively (using the two-band approach).

Using IMARE spectroscopy of SnS junctions made using the MCPBJ technique, the magnitudes and temperature dependences of the SC-order parameters ($\Delta_{L,S}(T)$) were determined locally and directly. A possible $A_L \approx (28$ –43)% anisotropy of the large SC gap was shown in the k space, which remained almost constant with temperature up to T_c .

The obtained characteristic ratio for the large SC gap is $2\Delta_L(0)/k_B T_c \approx 3.9$ –6.0 (the range corresponds to the possible Δ_L anisotropy), whereas that for the small SC gap is $2\Delta_S(0)/k_B T_c \approx 1.4$ –2.0 < 3.5, which is typical for a “weak” SC condensate in a multiple-band superconductor. Using two-band fit of the experimental $\Delta_{L,S}(T)$ curves, we estimated a quadruple of λ_{ij}^0 coupling constants and showed that it could be used in order to quantitatively fit the experimental $H_{c2}(T)$ with a two-band model, yielding a band diffusivity ratio of $D_1/D_2 \approx 3.5$ –3.8.

Author Contributions: Conceptualization, supervision and project administration, T.K.; resources, I.M., A.S. (Andrey Shilov) and Y.R.; methodology, L.M., S.K., I.M. and A.S. (Andrey Sadakov); investigation, all the authors; formal analysis, L.M., I.Z., A.S. (Andrey Shilov), Y.R., S.K., A.D. and

A.S. (Andrey Sadakov); writing—original draft preparation, L.M., I.M., A.D. and T.K.; writing—review and editing, L.M., I.M., S.K. and T.K. All authors have read and agreed to the published version of the manuscript.

Funding: This research was funded by the Russian Science Foundation (grant number 22-72-10082).

Institutional Review Board Statement: Not applicable.

Informed Consent Statement: Not applicable.

Data Availability Statement: The experimental data are available on demand.

Acknowledgments: This research was partly performed using the research equipment of the Shared facility center at P.N. Lebedev Physical Institute RAS.

Conflicts of Interest: The authors declare no conflict of interest.

Abbreviations

The following abbreviations are used in this manuscript:

SC	Superconducting
XRD	X-ray diffraction
BCS	Bardeen–Cooper–Schrieffer
WHH	Werthammer–Helfand–Hohenberg
AFM	Antiferromagnetism
ARPES	Angle-resolved photoemission spectroscopy
CVC	Current–voltage characteristic
IMARE	Incoherent multiple Andreev reflection effect
MCPBJ	Mechanically controlled planar break junction
SGS	Subharmonic gap structure
SnS	Superconductor–normal metal–superconductor
ZBC	Zero-bias conductance

Appendix A. IMARE Spectroscopy Details

Figure A1a shows the theoretical CVC and $dI(V)/dV$ of an SnS junction (based on a single-gap BCS superconductor) predicted by [28]. The data are calculated for a semiballistic regime ($l^{el}/d < 2$).

During IMARE, incoherent transport through the SnS junction (“long” contact regime) causes no supercurrent branch at $eV = 0$ in the CVC, contrary to the case of a “short” junction with $d < \xi$ and therefore with phase coherence between the SC banks, as described in [32,33]. Additionally, in the IMARE regime, an excess current (I_{exc}) appears within the whole bias voltage range, as compared to CVC in the normal state above T_c [28–31]. At high bias voltages, $I_{exc}(V)$ tends toward a constant value. In the case of a highly transparent metallic layer (transparency $> 80\%$, barrier strength $Z < 0.35$), dynamic conductance drastically rises at $eV \rightarrow 0$, forming a so-called “foot” area and an enhanced ZBC peak at $eV \rightarrow 0$ in the $dI(V)/dV$ spectrum [28,30,31].

A series of SGS features at positions $eV_n(T) = 2\Delta(T)/n$ ($n = 1, 2, \dots$) also appears in the $I(V)$ and $dI(V)/dV$ curves of the SnS junction below T_c [28,29,32,33]. For a highly transparent junction (typically observed in Na(Fe,Co)As (see Figures 6 and 7)), SGS represents a series of $dI(V)/dV$ dips (the dashed line in Figure A1a). The number (n^*) of observable SGS dips depends mainly on the ballistic l^{el}/d ratio [30,31]. Even minor occurrence of normal reflections (resulting in Z increase) and inelastic scattering reduce n^* . As a result, for the studied SnS junctions, one to two harmonics are visible in the $dI(V)/dV$: a fundamental one at $eV = 2\Delta$ and a second one at $eV = \Delta$.

With a temperature increase, all the IMARE features (I_{exc} , ZBC, and SGS) become less intensive and fully vanish at T_c . The position of the SGS shifts toward zero bias in accordance with the $\Delta(T)$ temperature dependence (see solid lines in Figure A1a).

The shape of the SGS features in the $dI(V)/dV$ curve strongly depends on the SC gap symmetry. Figure A1b shows typical Andreev dips calculated numerically in the

framework proposed in [34]. In the case of an isotropic SC gap with s -wave symmetry type, IMARE causes sharp and pronounced Andreev dips in the $dI(V)/dV$ spectrum (black line). For SC-order parameters with any nodal angle distribution ($\Delta(\theta)$, where θ is an angle in the momentum space), including the d -wave symmetry type, a strong suppression of the SGS dip intensity is expected (note, the amplitude of the blue line in Figure A1 is manually zoomed by a factor of 10 along the vertical axis for clarity). In the case of an anisotropic SC-order parameter with extended s -wave symmetry, each SGS subharmonic would represent a doublet. As an example, the angle distribution ($\Delta(\theta)$) of an SC gap with 30% anisotropy in the $k_x k_y$ plane (in the inset) and the corresponding doublet are shown in Figure A1 (magenta line).

In Figure A1c, a scheme of MCPBJ contact in the layered single crystal is presented. For such compounds, steps and terraces naturally appear on the cryogenic clefts (shown by gray areas on the top of Figure A1c). By gently tuning the sample holder curvature, the cryogenic clefts slide onto each other along the ab direction, touching through various terraces. As a result, the area (determining the normal resistance (R_N)) of the junction rather than the distance between the SC clefts (and therefore the barrier strength (Z)) is the adjustable parameter in our experimental setup. According to our estimates, the typical size of the MCPBJ contact is about 10–50 nm along the ab plane [51,52].

Generally, the crack is located in the bulk of the sample and far from current and potential leads. The MCPBJ contact is not fully opened, preventing the penetration of impurities into the crack and degradation of the superconducting properties on their surface, in addition to minimizing overheating of the junction during the current flow. For more details, see [36].

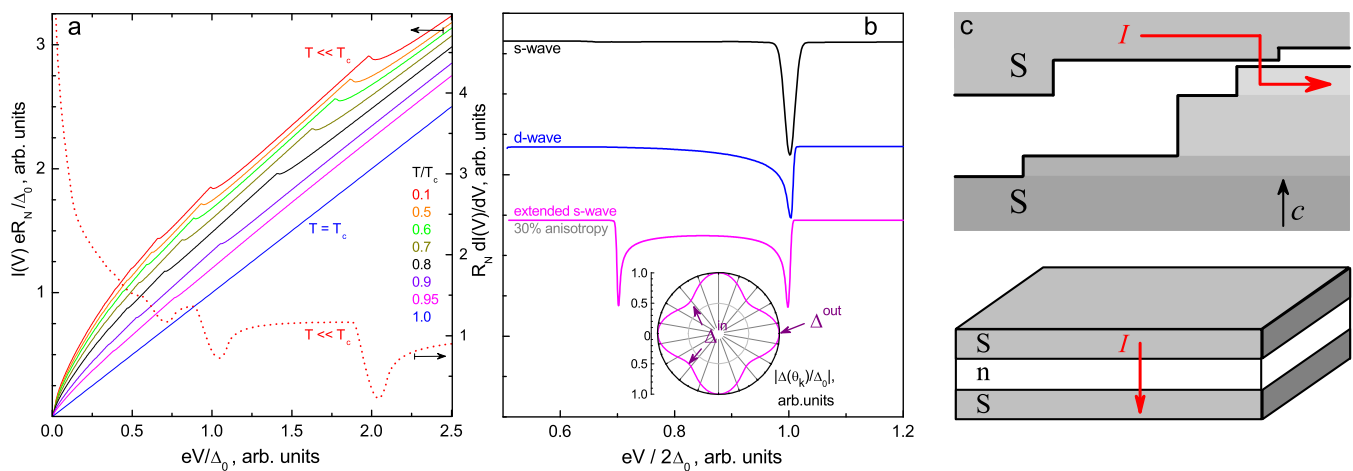


Figure A1. (a) Temperature evolution of the CVC of an SnS junction in the IMARE regime (left vertical axis) and the corresponding dynamic conductance spectrum at $T \ll T_c$ (right axis) calculated in the framework proposed in [28]. (b) Typical shape of an Andreev feature in the $dI(V)/dV$ spectrum for the case of an isotropic SC gap with s -wave symmetry (black line), d -wave symmetry (blue line; the raw data are zoomed vertically by a factor of 10 for clarity), and extended s -wave symmetry with 30% anisotropy (magenta line). The data were numerically calculated using the approach proposed in [34]. For the latter case, the related SC gap angle distribution (Δ_θ) is shown in the inset. (c) Scheme of a planar break junction typically obtained in the layered single crystal.

References

1. Wang, X.C.; Liu, Q.Q.; Lv, Y.X.; Gao, W.B.; Yang, L.X.; Yu, R.C.; Li, F.Y.; Jin, C.Q. The superconductivity at 18 K in LiFeAs system. *Solid State Commun.* **2008**, *148*, 538. [CrossRef]
2. Parker, D.R.; Pitcher, M.J.; Baker, P.J.; Franke, I.; Lancaster, T.; Blundell, S.J.; Clarke S.J. Structure, antiferromagnetism and superconductivity of the layered iron arsenide NaFeAs. *Chem. Commun.* **2009**, *2009*, 2189. [CrossRef]
3. Kuzmicheva, T.E.; Kuzmichev, S.A. Electron and Superconducting Properties of the AFeAs (A= Li, Na) Family Alkali-Metal Pnictides: Current Stage of the Research (mini-review). *JETP Lett.* **2021**, *114*, 630. [CrossRef]

4. Wang, A.F.; Luo, X.G.; Yan, Y.J.; Ying, J.J.; Xiang, Z.J.; Ye, G.J.; Cheng, P.; Li, Z.Y.; Hu, W.J.; Chen, X.H. Phase diagram and calorimetric properties of $\text{NaFe}_{1-x}\text{Co}_x\text{As}$. *Phys. Rev. B* **2012**, *85*, 224521. [[CrossRef](#)]
5. Tan, G.; Zheng, P.; Wang, X.; Chen, Y.; Zhang, X.; Luo, J.; Netherton, T.; Song, Y.; Dai, P.; Zhang, C.; et al. Strong-coupling superconductivity in $\text{NaFe}_{1-x}\text{Co}_x\text{As}$: Validity of Eliashberg theory. *Phys. Rev. B* **2013**, *87*, 144512. [[CrossRef](#)]
6. Steckel, F.; Roslova, M.; Beck, R.; Morozov, I.; Aswartham, S.; Evtushinsky, D.; Blum, C.G.M.; Abdel-Hafiez, M.; Bombor, D.; Maletz, J.; et al. Crystal growth and electronic phase diagram of 4d-doped $\text{Na}_{1-\delta}\text{Fe}_{1-x}\text{Rh}_x\text{As}$ in comparison to 3d-doped $\text{Na}_{1-\delta}\text{Fe}_{1-x}\text{Co}_x\text{As}$. *Phys. Rev. B* **2015**, *91*, 184516. [[CrossRef](#)]
7. Wright, J.D.; Lancaster, T.; Franke, I.; Steele, A.J.; Möller, J.S.; Pitcher, M.J.; Corkett, A.J.; Parker, D.R.; Free, D.G.; Pratt, F.L.; et al. Gradual destruction of magnetism in the superconducting family $\text{NaFe}_{1-x}\text{Co}_x\text{As}$. *Phys. Rev. B* **2012**, *85*, 054503. [[CrossRef](#)]
8. Parker, D.R.; Smith, M.J.P.; Lancaster, T.; Steele, A.J.; Franke, I.; Baker, P.J.; Pratt, F.L.; Pitcher, M.J.; Blundell, S.J.; Clarke, S.J. Control of the Competition between a Magnetic Phase and a Superconducting Phase in Cobalt-Doped and Nickel-Doped NaFeAs Using Electron Count. *Phys. Rev. Lett.* **2010**, *104*, 057007. [[CrossRef](#)]
9. Wang, A.F.; Ying, J.J.; Luo, X.G.; Yan, Y.J.; Liu, D.Y.; Xiang, Z.J.; Cheng, P.; Ye, G.J.; Zou, L.J.; et al. A crossover in the phase diagram of $\text{NaFe}_{1-x}\text{Co}_x\text{As}$ determined by electronic transport measurements. *N. J. Phys.* **2013**, *15*, 043048. [[CrossRef](#)]
10. Watson, M.D.; Aswartham, S.; Rhodes, L.C.; Parrett, B.; Iwasawa, H.; Hoesch, M.; Morozov, I.; Büchner, B.; Kim, T.K. Three-dimensional electronic structure of the nematic and antiferromagnetic phases of NaFeAs from detwinned angle-resolved photoemission spectroscopy. *Phys. Rev. B* **2018**, *97*, 035134. [[CrossRef](#)]
11. Liu, Z.-H.; Richard, P.; Nakayama, K.; Chen, G.-F.; Dong, S.; He, J.-B.; Wang, D.-M.; Xia, T.-L.; Umezawa, K.; Kawahara, T.; et al. Unconventional superconducting gap in $\text{NaFe}_{0.95}\text{Co}_{0.05}\text{As}$ observed by angle-resolved photoemission spectroscopy. *Phys. Rev. B* **2011**, *84*, 064519. [[CrossRef](#)]
12. Ge, Q.Q.; Ye, Z.R.; Xu, M.; Zhang, Y.; Jiang, J.; Xie, B.P.; Song, Y.; Zhang, C.L.; Dai, P.; Feng, D.L. Anisotropic but Nodeless Superconducting Gap in the Presence of Spin-Density Wave in Iron-Pnictide Superconductor $\text{NaFe}_{1-x}\text{Co}_x\text{As}$. *Phys. Rev. X* **2013**, *3*, 011020.
13. Cai, P.; Zhou, X.; Ruan, W.; Wang, A.; Chen, X.; Lee, D.-H.; Wang, Y. Visualizing the microscopic coexistence of spin density wave and superconductivity in underdoped $\text{NaFe}_{1-x}\text{Co}_x\text{As}$. *Nat. Commun.* **2013**, *4*, 1596. [[CrossRef](#)]
14. Yang, H.; Wang, Z.; Fang, D.; Li, S.; Kariyado, T.; Chen, G.; Ogata, M.; Das, T.; Balatsky, A.V.; Wen, H.-H. Unexpected weak spatial variation in the local density of states induced by individual Co impurity atoms in superconducting $\text{Na}(\text{Fe}_{1-x}\text{Co}_x)\text{As}$ crystals revealed by scanning tunneling spectroscopy. *Phys. Rev. B* **2012**, *86*, 214512. [[CrossRef](#)]
15. Mazin, I.I.; Singh, D.J.; Johannes, M.D.; Du, M.H. Unconventional sign-reversing superconductivity in $\text{LaFeAsO}_{1-x}\text{F}_x$. *Phys. Rev. Lett.* **2008**, *101*, 057003. [[CrossRef](#)]
16. Kontani, H.; Onari, S. Orbital-Fluctuation-Mediated Superconductivity in Iron Pnictides: Analysis of the Five-Orbital Hubbard-Holstein Model. *Phys. Rev. Lett.* **2010**, *86*, 157001. [[CrossRef](#)]
17. Onari, S.; Kontani, H. Hidden antiferromagnetic order in Fe-based superconductor BaFe_2As_2 and NaFeAs above T_S . *Phys. Rev. Res.* **2020**, *2*, 042005(R). [[CrossRef](#)]
18. Hirschfeld, P.J. Using gap symmetry and structure to reveal the pairing mechanism in Fe-based superconductors. *C. R. Physique* **2016**, *17*, 197. [[CrossRef](#)]
19. Yu, R.; Zhu, J.-X.; Si, Q. Orbital-selective superconductivity, gap anisotropy, and spin resonance excitations in a multiorbital $t - J_1 - J_2$ model for iron pnictides. *Phys. Rev. B* **2014**, *89*, 024509. [[CrossRef](#)]
20. Saito, T.; Onari, S.; Kontani, H. Nodal gap structure in Fe-based superconductors due to the competition between orbital and spin fluctuations. *Phys. Rev. B* **2013**, *88*, 045115. [[CrossRef](#)]
21. Wang, Y.; Kreisel, A.; Zabolotnyy, V.B.; Borisenko, S.V.; Büchner, B.; Maier, T.A.; Hirschfeld, P.J.; Scalapino, D.J. Superconducting gap in LiFeAs from three-dimensional spin-fluctuation pairing calculations. *Phys. Rev. B* **2013**, *88*, 174516. [[CrossRef](#)]
22. Kreisel, A.; Andersen, B.M.; Sprau, P.O.; Kostin, A.; Seamus Davis, J.C.; Hirschfeld, P.J. Orbital selective pairing and gap structures of iron-based superconductors. *Phys. Rev. B* **2017**, *95*, 174504. [[CrossRef](#)]
23. Saito, T.; Onari, S.; Yamakawa, H.; Kontani, H.; Borisenko, S.V.; Zabolotnyy, V.B. Reproduction of experimental gap structure in LiFeAs based on orbital-spin fluctuation theory: s^{++} -wave, s^{\pm} -wave, and hole- s^{\pm} -wave states. *Phys. Rev. B* **2014**, *90*, 035104. [[CrossRef](#)]
24. Saito, T.; Yamakawa, H.; Onari, S.; Kontani, H. Revisiting orbital-fluctuation-mediated superconductivity in LiFeAs : Nontrivial spin-orbit interaction effects on the band structure and superconducting gap function. *Phys. Rev. B* **2015**, *92*, 134522. [[CrossRef](#)]
25. Spyrisson, N.; Tanatar, M.A.; Cho, K.; Song, Y.; Dai, P.; Zhang, C.; Prozorov, R. Environmental stability and anisotropic resistivity of Co-doped $\text{Na}_{1-\delta}\text{Fe}_{1-x}\text{Co}_x\text{As}$. *Phys. Rev. B* **2012**, *86*, 144528. [[CrossRef](#)]
26. Ghannadzadeh, S.; Wright, J.D.; Foronda, F.R.; Blundell, S.J.; Clarke, S.J.; Goddard, P.A. Upper critical field of $\text{NaFe}_{1-x}\text{Co}_x\text{As}$ superconductors. *Phys. Rev. B* **2014**, *89*, 054502. [[CrossRef](#)]
27. Ahmad, D.; Choi, W.J.; Sonora, D.; Oh, Y.S.; Mosqueira, J.; Park, T.; Kwon, Y.S. Anisotropy dependence of the fluctuation spectroscopy in the critical and gaussian regimes in superconducting $\text{NaFe}_{1-x}\text{Co}_x\text{As}$ single crystals. *Sci. Rep.* **2018**, *8*, 8556. [[CrossRef](#)] [[PubMed](#)]
28. Kümmel, R.; Günsenheimer, U.; Nicolisky, R. Andreev scattering of quasiparticle wave packets and current-voltage characteristics of superconducting metallic weak links. *Phys. Rev. B* **1990**, *42*, 3992. [[CrossRef](#)] [[PubMed](#)]

29. Octavio, M.; Tinkham, M.; Blonder, G.E.; Klapwijk, T.M. Subharmonic energy-gap structure in superconducting constrictions. *Phys. Rev. B* **1983**, *27*, 6739. [[CrossRef](#)]
30. Gunsenheimer, U.; Zaikin, A.D. Ballistic charge transport in superconducting weak links. *Phys. Rev. B* **1994**, *50*, 6317. [[CrossRef](#)]
31. Gunsenheimer, U.; Zaikin, A.D. Ballistic charge transport in superconducting weak links in a microwave field. *Europhys. Lett.* **1998**, *41*, 195. [[CrossRef](#)]
32. Arnold, G.B. Superconducting Tunneling without the Tunneling Hamiltonian. II. Subgap Harmonic Structure. *J. Low. Temp. Phys.* **1987**, *68*, 1–27. [[CrossRef](#)]
33. Averin, D.; Bardas, A. ac Josephson Effect in a Single Quantum Channel. *Phys. Rev. Lett.* **1995**, *75*, 1831. [[CrossRef](#)]
34. Devereaux, T.P.; Fulde, P. Multiple Andreev scattering in superconductor-normal metal-superconductor junctions as a test for anisotropic electron pairing. *Phys. Rev. B* **1993**, *47*, 14638. [[CrossRef](#)] [[PubMed](#)]
35. Moreland, J.; Ekin, J.W. Electron tunneling experiments using Nb?Sn “break” junctions. *J. Appl. Phys.* **1985**, *58*, 3888. [[CrossRef](#)]
36. Kuzmichev, S.A.; Kuzmicheva, T.E. “Break-junction” technique in application to layered superconductors. *Low Temp. Phys.* **2016**, *42*, 1008. [[CrossRef](#)]
37. Liu, Z.-H.; Richard, P.; Li, Y.; Jia, L.-L.; Chen, G.-F.; Xia, T.-L.; Wang, D.-M.; He, J.-B.; Yang, H.-B.; Pan, Z.-H.; et al. Orbital characters and near two-dimensionality of Fermi surfaces in NaFe_{1-x}Co_xAs. *Appl. Phys. Lett.* **2012**, *101*, 202601. [[CrossRef](#)]
38. Cui, S.T.; Zhu, S.Y.; Wang, A.F.; Kong, S.; Ju, S.L.; Luo, X.G.; Chen, X.H.; Zhang, G.B.; Sun, Z. Evolution of the band structure of superconducting NaFeAs from optimally doped to heavily overdoped Co substitution using angle-resolved photoemission spectroscopy. *Phys. Rev. B* **2012**, *86*, 155143. [[CrossRef](#)]
39. Deng, S.; Köhler, J.; Simon, A. Electronic structure and lattice dynamics of NaFeAs. *Phys. Rev. B* **2009**, *80*, 214508. [[CrossRef](#)]
40. Kusakabe, K.; Nakanishi, A. First-Principles Study of NaFeAs, NaCoAs, and NaNiAs. *J. Phys. Soc. Jpn.* **2009**, *12*, 124712. [[CrossRef](#)]
41. Tanatar, M.A.; Spyrison, N.; Cho, K.; Blomberg, E.C.; Tan, G.; Dai, P.; Zhang, C.; Prozorov, R. Evolution of normal and superconducting properties of single crystals of Na_{1-δ}As upon interaction with environment. *Phys. Rev. B* **2012**, *85*, 014510. [[CrossRef](#)]
42. Weickert, F.; Nicklas, M.; Schnelle, W.; Wosnitza, J.; Leithe-Jasper, A.; Rosner, H. Enhancement of the upper critical field in codoped iron-arsenic high-temperature superconductors. *J. Appl. Phys.* **2011**, *110*, 123906. [[CrossRef](#)]
43. Werthamer, N.R.; Helfand, E.; Hohenberg, P.C. Temperature and Purity Dependence of the Superconducting Critical Field, H_{c2} . III. Electron Spin and Spin-Orbit Effects. *Phys. Rev.* **1966**, *147*, 295. [[CrossRef](#)]
44. Gurevich A. Limits of the upper critical field in dirty two-gap superconductors. *Physica C* **2007**, *456*, 160. [[CrossRef](#)]
45. Kuzmichev, S.A.; Morozov, I.V.; Shilov, A.I.; Rakhmanov, E.O.; Kuzmicheva, T.E. Multiple Andreev Reflection Effect Spectroscopy of Underdoped NaFe_{1-x}Co_xAs Single Crystals. *JETP Lett.* **2023**, *117*, 612. [[CrossRef](#)]
46. Giaever, I.; Megerle, K. Study of Superconductors by Electron Tunneling. *Phys. Rev.* **1961**, *122*, 1101. [[CrossRef](#)]
47. Moskalenko, V.A. Superconductivity of metals considering the overlapping of energy bands. *Phys. Met. Metallogr.* **1959**, *8*, 25.
48. Moskalenko, V.A. Temperature and Purity Dependence of the Superconducting Critical Field, H_{c2} . The Theory of Superconductors with Overlapping Energy Bands. *Sov. Phys. Usp.* **1974**, *17*, 450. [[CrossRef](#)]
49. Suhl, H.; Matthias, B.T.; Walker, L.R. Bardeen-Cooper-Schrieffer Theory of Superconductivity in the Case of Overlapping Bands. *Phys. Rev. Lett.* **1959**, *3*, 552. [[CrossRef](#)]
50. Kuzmicheva, T.E.; Kuzmichev, S.A. Characteristics of superconducting subsystems in magnesium diborides and iron oxypnictides from data on spectroscopy of multiple Andreev reflections. *Low Temp. Phys.* **2019**, *45*, 1161. [[CrossRef](#)]
51. Kuzmichev, S.; Kuzmicheva, T.; Morozov, I.; Boltalin, A.; Shilov, A. Multiple Andreev reflections effect spectroscopy of LiFeAs single crystals: Three superconducting order parameters and their temperature evolution. *SN Appl. Sci.* **2022**, *4*, 189. [[CrossRef](#)]
52. Kuzmicheva, T.E.; Kuzmichev, S.A.; Pervakov, K.S.; Vlasenko, V.A. Superconducting order parameters in overdoped BaFe_{1.86}Ni_{0.14}As₂ revealed by multiple Andreev reflection spectroscopy of planar break junctions. *Phys. Rev. B* **2021**, *104*, 174512. [[CrossRef](#)]
53. Boeri, L.; Dolgov, O.V.; Golubov, A.A. Is LaFeAsO_{1-x}F_x an Electron-Phonon Superconductor? *Phys. Rev. Lett.* **2008**, *101*, 026403. [[CrossRef](#)] [[PubMed](#)]
54. Wong, C.H.; Lortz, R. Preliminary T_c Calculations for Iron-Based Superconductivity in NaFeAs, LiFeAs, FeSe and Nanostructured FeSe/SrTiO₃ Superconductors. *Materials* **2023**, *16*, 4674. [[CrossRef](#)] [[PubMed](#)]

Disclaimer/Publisher’s Note: The statements, opinions and data contained in all publications are solely those of the individual author(s) and contributor(s) and not of MDPI and/or the editor(s). MDPI and/or the editor(s) disclaim responsibility for any injury to people or property resulting from any ideas, methods, instructions or products referred to in the content.